Acoustic Boundary Layers in Solid Propellant Rocket Motors Using Navier-Stokes Equations

F. Vuillot* and G. Avalon†
Office National d'Etudes et de Recherches Aérospatiales, Châtillon, France

The numerical solution of laminar, two-dimensional, compressible, and unsteady Navier-Stokes equations is aimed at a complete description of acoustic boundary layers that develop above a burning propellant. Such acoustic boundary layers can be responsible for the so-called flow turning losses. They can govern the local unsteady flow conditions that are seen by the burning propellant to which it finally responds. In those respects, a complete understanding of such acoustic boundary layers is essential to improve existing solid rocket stability prediction codes. The full numerical solution of the Navier-Stokes equations incorporates into the analysis all the features of two-dimensional rocket chamber mean flowfield in a natural manner. After a standing wave pattern is established through forcing at a given frequency, a special Fourier treatment is used to transform the numerical results in a form directly comparable to available linear acoustic data. The presented results indicate that the acoustic boundary layer is substantially thinner than predicted by simplified models. Moreover, its acoustic admittance is found to vary significantly along the chamber, a result that is of major importance to stability predictions. Finally, the acoustic field is found to be rotational over a significant volume of the chamber.

Nomenclature

a = speed of sound
A = excitation amplitude
$A(\ )$ = amplitude, or modulus of a complex quantity
$\mathcal{A}$ = grid cell area
C_p, C_v = constant pressure, volume specific heats
E = total specific internal energy, $E = C_vT + (u^2 + v^2)/2$
FT = complex Fourier component at excitation frequency of a time varying quantity
f = frequency
h = chamber half-height
i = complex number, $i = \sqrt{-1}$
k = thermal conductivity
L = chamber length
M = Mach number
n = unit normal vector
Pr = Prandtl number, $Pr = \mu C_p/k$
p = pressure
r = perfect gas constant
$(Re)_0$ = reference Reynolds number, $(Re)_0 = \rho_0 a_0 L/\mu_0$
T = temperature or time period of an oscillation
t = time
U = column vector of conservative flow variables
u = axial flow velocity
v = transverse or normal flow velocity
x = axial coordinate
Y = dimensionless acoustic admittance, $Y = \rho_0 a_0 v'/\gamma p'$
y = transverse coordinate
γ = ratio of specific heats
λ = coefficient of bulk viscosity
μ = dynamic viscosity
ν = kinematic viscosity
ρ = density
σ_x, σ_y = normal stresses
τ_{xy}, τ_{yx} = shear stresses
$\Phi(\ )$ = argument of a complex quantity or phase angle (expressed in degrees)
ω = angular frequency
Ω = vorticity

Subscripts, Superscripts
$(\ )_0$ = reference state
$\bar{(\ )}$ = steady-state value
$(\ )'$ = unsteady component
$(\ )_{inj}$ = injection
$(\ )_i$ = stagnation value

Received June 2, 1988; presented as Paper 88-2940 at the AIAA/ASME/SAE/ASEE 24th Joint Propulsion Conference, Boston, MA, July 11-13, 1988; revision received Oct. 10, 1989.

*Research Engineer, Energetics Department. Member AIAA.
†Head of Research Group, Energetics Department.

Introduction

In recent years, considerable attention has been given to multidimensional flow processes taking place inside solid propellant combustion chambers because they are believed to be critical to rocket motor stability. In particular, the unsteady or acoustic boundary layer that develops above the burning propellant appears to be an important feature of rocket stability. Indeed, such a boundary layer controls the energy exchange between the oscillatory and steady motions and also governs the local instantaneous flow conditions that are seen by the burning propellant and to which it finally responds. In that respect, complete understanding of acoustic boundary-layer behavior seems essential before arriving at any velocity coupling model.

At the present time, most stability prediction codes are based on the acoustic balance approach proposed by Hart and McClure many years ago.[1] This approach is based on linearized inviscid equations and has been extended into a quite general and practicable form by Culick.[2,3] In that process, Culick noted that one-dimensional analyses exhibited a large damping source that was absent from three-dimensional analyses. Culick linked this damping to viscous boundary layers and termed it "flow turning" by reference to the turning of the flow from a side injection to axial direction (more precisely, it is the resulting orthogonality between the mean injection velocity and acoustic velocity that matters). However, Culick's approximation of viscous acoustic loss relied on an inviscid approach and has been contested [e.g., see Ref. (4)].

Flandro[5] first considered the actual behavior of acoustic boundary layers above an injecting wall by solving the unsteady boundary-layer equations in the case of a one-dimensional mean flow (perpendicular to the injecting wall). He demonstrated that for a grazing acoustic wave, such an acoustic boundary layer was responsible for the flow turning loss. The appropriateness of Flandro's approach has been demonstrated on a small laboratory rocket motor.[6] The major drawback of Flandro's analysis lies in the acoustic boundary-layer thickness. Indeed, calculations show that due to the massive blowing from the burning propellant, the acoustic boundary layer extends to the core of the flow where the mean velocity field becomes more axially oriented. This obviously violates the assumption of a pure normal mean flow.

One of the objectives of the present work is precisely to relax such oversimplified assumptions. Flandro's simple linear analytical approach, although oversimplifying the characteristics of the mean flowfield, was very useful in the sense that it helped understanding the fluid mechanics associated with flow turning. A first step towards a better description of the mean flow is proposed by Hegde et al.,[7] who retained a $\partial\bar{u}/\partial y$ term, in the linearized equations. This led to results similar to Flandro's, except near pressure nodes where the boundary-layer admittance was found to depend on the axial coordinate.

To further describe the unsteady flow processes without analytical complexities, direct multidimensional numerical simulations of full unsteady Navier-Stokes equations must be employed. Baum and Levine[8,9] presented some computations performed by means of an implicit Navier-Stokes solver with a modified (k,ϵ) turbulence model.

Although the present work is not directly concerned with velocity coupling, it must be noted that, doubtlessly, acoustic boundary layers are a key feature in the response of a burning propellant to velocity oscillations. When dealing with velocity coupling, it should be noted that at least two mechanisms are believed to lead to a velocity coupled response. One possible mechanism can be thought of as a mere perturbation of an erosive burning regime by the velocity oscillations. More recent interpretations of velocity coupling call for an intimate coupling between unsteady flow processes and gas phase combustion. These authors believe that both mechanisms are physically sound and may prevail according to chamber conditions. An example of the first kind of velocity coupling was recently demonstrated at ONERA and is reported in Ref. 10. These results showed that the modulus of the observed velocity response function could be correctly predicted by an unsteady erosive burning model,[11] while the phase relationship could not be completely explained. The other kind of velocity coupling, which has been quite often reported in the literature (e.g., barrel type burning), has been the subject of recent modeling efforts. These advanced models incorporate a simplified gas flame kinetics in the gas phase equation. The works of T'ien[12] and later on Flandro[13] used a simplified kinetics in the form of a one-step second-order premixed gas flame and developed the equations in powers of the wave amplitude. T'ien only considered the case of an end burning propellant submitted to normal wave incidence and limited his development to first order. He demonstrated that the unsteadiness of the gas flame was responsible for a secondary peak in the pressure coupled response function, which resulted in some damping at high frequencies.

More recently, Flandro[13] revisited T'ien's approach by including momentum effects of grazing incidence and developing the equations up to second-order in wave amplitude. T'ien's results were recovered, and no linear velocity coupling was found to appear until very high frequencies. However, no turbulence modeling or unsteady transition were introduced in this work. In recent publications, Beddini et al.[14] pinpointed the possible acoustic-combustion interactions through nonlinear effects or acoustically generated turbulence.

Cold flow experiments by Brown et al.[15,16] demonstrated the complexity of the unsteady velocity field and the influence of mean flow turbulence on the oscillatory heat flux received by the injecting wall. At low acoustic amplitude, they demonstrated that the mean flow turbulence had a shielding effect against acoustic signal propagation to the wall. At higher amplitude, nonlinear effects were demonstrated. The velocity field was found to be rotational over a significant volume of the chamber, in qualitative agreement with acoustic boundary-layer analysis. The modification brought by this rotational nature to the acoustic balance approach is presented in Ref. 16. It is believed that the present work can shed new light on the present debate on velocity coupling, although gas phase kinetics, as well as an ad hoc turbulence modeling, have yet to be incorporated.

Finally and aside from the flow turning and velocity coupling debates, the present work and the work reported in Ref. 18 can be understood as preliminary steps toward numerical simulation of a full motor unsteady flowfield that can now be envisioned due to the progress made in computer speed and memory.

Computational Model Development

The present numerical effort is primarily intended to complement previous analytical works describing the unsteady flowfield inside a solid propellant rocket chamber.[5] The numerical technique permits relaxing major assumptions relative to the mean flowfield that was needed by analytical approaches. To avoid numerical difficulties, the simple test case of a rectangular chamber is first considered. It should be mentioned that this particular geometry has also been retained with reference to the geometry of the experimental apparatus used in Ref. 10. A computer code that solves the full unsteady, compressible, two-dimensional, laminar Navier-Stokes equations has been written.

The equations, in conservative vector form, read as follows:

$$\frac{\partial U}{\partial t}+\frac{\partial F}{\partial x}+\frac{\partial G}{\partial y}=0$$

where

$$U=\begin{bmatrix}\rho\\ \rho u\\ \rho v\\ \rho E\end{bmatrix},\qquad F=\begin{bmatrix}\rho u\\ \rho u^2+\sigma_x\\ \rho uv+\tau_{xy}\\ (\rho E+\sigma_x)u+\tau_{yx}v-k\partial T/\partial x\end{bmatrix}$$

$$G=\begin{bmatrix}\rho v\\ \rho uv+\tau_{yx}\\ \rho v^2+\sigma_y\\ (\rho E+\sigma_y)v+\tau_{xy}u-k\partial T/\partial y\end{bmatrix}$$

with

$$\sigma_x=p-\lambda\left(\frac{\partial u}{\partial x}+\frac{\partial v}{\partial y}\right)-2\mu\frac{\partial u}{\partial x}$$

$$\sigma_y=p-\lambda\left(\frac{\partial u}{\partial x}+\frac{\partial v}{\partial y}\right)-2\mu\frac{\partial u}{\partial y}$$

$$\tau_{xy}=\tau_{yx}=-\mu\left(\frac{\partial u}{\partial y}+\frac{\partial v}{\partial x}\right)$$

Stokes' hypothesis is used to express the bulk viscosity coefficient:

$$\lambda=-\tfrac{2}{3}\mu$$

and the perfect gas law is used

$$p=r\rho T$$

For numerical treatment, these equations are put in dimensionless form by using the following reference values. Then the velocities are divided by the reference speed of sound a_0, lengths by the chamber length L, time by L/a_0, density by ρ_0, temperature by T_0 (usually the injection temperature), and pressure by $\rho_0 a_0^2$.

The numerical scheme is a finite-volume version of the explicit predictor-corrector McCormack scheme. The equations are directly discretized in the physical plane. The solution at the center of grid cell (i,j) and at time $(n+1)\Delta t$ is computed from the flux balance through grid cell faces, in the following way:

$$\tilde{U}_{ij}^{n+1} = U_{ij}^n - \frac{\Delta t}{\mathcal{A}_{ij}} \sum_{k:4 \text{ sides}} \left[F_k^{\pm} \ell_k \boldsymbol{n}_k \cdot \boldsymbol{i}_x + G_k^{\pm} \ell_k \boldsymbol{n}_k \cdot \boldsymbol{i}_y \right]^n$$

$$U_{ij}^{n+1} = \frac{1}{2}\left\{ U_{ij}^n + \tilde{U}_{ij}^{n+1} - \frac{\Delta t}{\mathcal{A}_{ij}} \sum_k \left[F_k^{\mp} \ell_k \boldsymbol{n}_k \cdot \boldsymbol{i}_x + G_k^{\mp} \ell_k \boldsymbol{n}_k \cdot \boldsymbol{i}_y \right]^{\tilde{n+1}} \right\}$$

and k is a summation indice that indicates the four grid cell faces of length ℓ_k. Superscripts + and − indicate forward and backward flux evaluations. The +, − sequence is alternated at each time step.

No turbulence modeling has yet been introduced due to the lack of models directly applicable to steady and unsteady internal rocket flows. Preliminary testing and adapting of candidate models is needed. It is believed that the absence of turbulence model in the present work is a conservative measure. Indeed the computed results are free of possible bias introduced by inappropriate turbulence modeling. Moreover, remaining laminar permits one to analyze two-dimensional results by direct comparison with Flandro's simplified analysis.[5] The numerical tools have been validated against inviscid steady and unsteady nozzle flows, as well as on nozzleless rocket motor internal transonic flows and have given good results.[17,18] For steady flow computations, convergence is accelerated by means of a local time step procedure. Of course this procedure is turned off for unsteady computations. Extensive testing has been done to check the unsteady behavior of the scheme. It appeared that, as already noted by Baum and Levine,[19] noncontinuous solutions (e.g., traveling shocked waves) were not properly handled by the scheme. However, good properties have been demonstrated for smooth solutions over a wide Courant Freidrich and Levy (CFL) number range, provided that at least 20 grid points per wave length were available.[18] This conclusion is similar to results published by other researchers for a Lax-Wendroff scheme.[20]

Computations were performed for the lower half of a rectangular chamber with bottom side injection. No artificial viscosity has been added to the numerical scheme; time steps have usually been taken to be 0.6 times the maximum CFL stability criterion time step. All spurious numerical oscillations, which developed during preliminary computer runs, have been suppressed by improved treatments of boundary conditions.

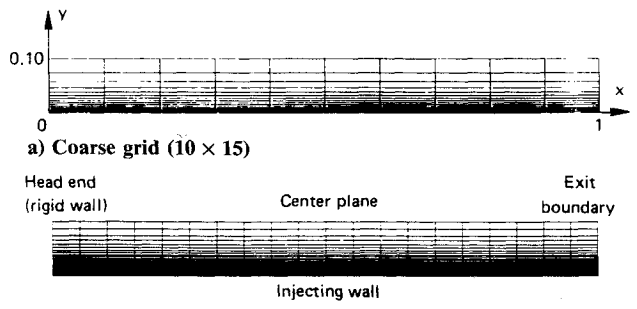

a) Coarse grid (10 × 15)

b) Fine grid (20 × 30)

Fig. 1 Geometry and grids for numerical computations.

The chamber half-height to length (h/L) ratio was taken to be 0.10. The two grids used for the present computations are displayed in Figs. 1a and 1b. The first is a coarse (10 × 15) grid with points concentrated near the injection surface where large gradients are anticipated. The ratio of the heights of the largest to the finest cell is approximately 10. This grid has been used for steady-state computations and preliminary unsteady computations. The second grid is a (20 × 30) grid obtained by dividing each cell of the coarse grid into four smaller cells. This refined grid has been used for the unsteady computations presented in this paper. The general boundary conditions were slip condition on the left, head-end, rigid wall boundary, symmetry on the upper, center plane boundary, constant mass flow rate, stagnation temperature and zero tangential velocity on the injecting surface, and static pressure condition at the right, outflow boundary.

Steady-State Solution

Before performing unsteady computations, an initial condition corresponding to a steady-state solution has to be evaluated. For that purpose, the computations are started from rest (uniform pressure, uniform temperature, zero velocity) and carried out for a given injection mass flow rate until a steady-state solution is attained.

A specially written outflow boundary condition subroutine is essential to this initialization (chamber pressurization) task. For an assumed ejection nozzle throat area and the exiting flow mean (averaged across the chamber height) properties (mass flow rate, dynalpy, and total enthalpy), this routine determines, at each time step, whether the assumed nozzle is choked or unchoked. The static pressure to be imposed at the chamber exit plane is computed accordingly. Before the nozzle becomes critical (which happens for a critical exit mass flow rate), ambient, or reference, conditions are assumed to exist at the nozzle throat. For critical or supercritical nozzle conditions, the outflow static pressure is derived from the critical exit mean Mach number and the outflow mean properties.

The steady-state computation was performed on the coarse grid with inviscid (Euler) equations for the following dimensionless conditions: injection mass flow rate: $(\rho v)_{inj}/\rho_0 a_0 = 0.036$; injection stagnation temperature: $T_i/T_0 = 1$; outflow static pressure $(p/\rho_0 a_0^2)$ = simulating a nozzle with an inlet to throat area ratio of 6; and $\gamma = 1.20$.

The inviscid equations can be safely used for this part of the computation since a good approximation of a steady-state solid rocket internal flowfield is given by an inviscid rotational solution.[17,21,22] A steady-state regime was attained after 70,000 time steps (45 min of CPU on a Control Data Corporation Cyber 855). Then, the solution was corrected through a few iterations with the viscous equations for a reference Reynolds number $Re = \rho_0 a_0 L/\mu_0$ of 3×10^4 and a Prandtl number of 1.0. It should be emphasized that dimensional quantities only enter the present analysis through Re.

Both inviscid and viscous steady-state solutions exactly recovered the well-known incompressible "cosine" velocity profiles[17,21,22] for a two-dimensional planar chamber with an exit mean Mach number of 0.10. At this point, a special piece of software allows one to obtain the solution on the twice-refined grid (fine grid). Simple bilinear interpolations are used to evaluate the solution at the center of every fine grid cell. A few more iterations are needed in the refined grid to eliminate the small errors resulting from the refinement procedure. This procedure was devised to save computer time by using fine grids only when needed (here to capture large unsteady gradients). Head-end steady-state results of interest to unsteady computations are $\bar{p}/p_0 = 3.67$, $\bar{\rho}/\rho_0 = 3.67$, $\bar{T}/T_0 = 1$, and $\bar{M}_{inj} = 0.00981$.

Unsteady Computations

The converged steady-state solution on a given grid is now used as an initial condition for the unsteady computations. The viscous equations are used, and the outflow static pres-

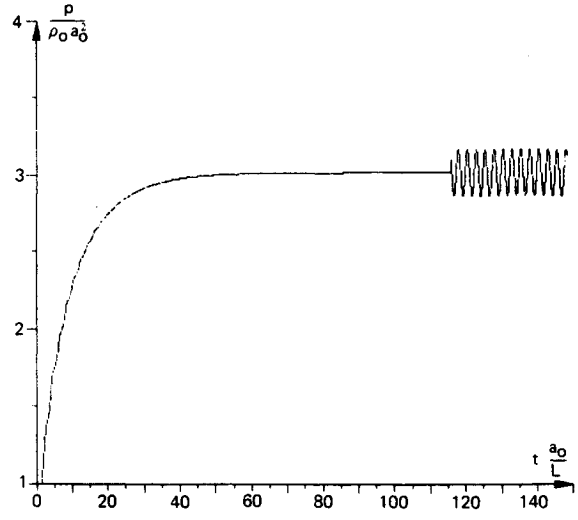

Fig. 2 Time history of aft-end static pressure.

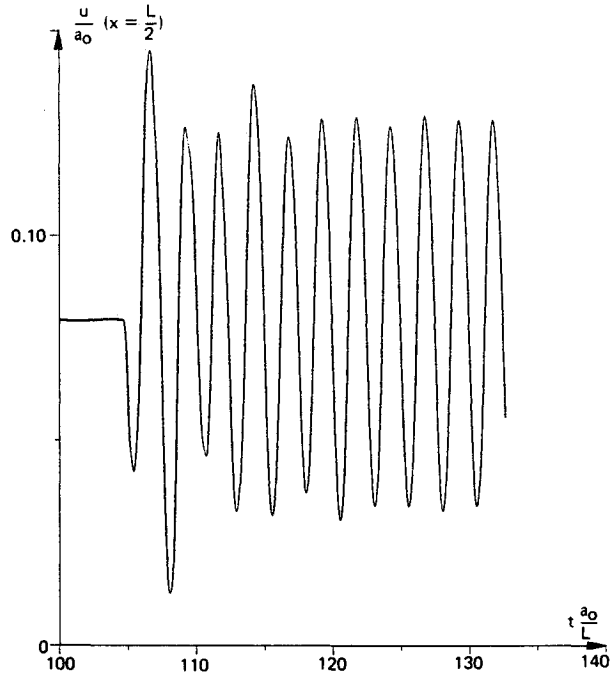

Fig. 3 Time history of axial velocity at chamber midlength (excitation starts at $T = 104.3$).

sure is sinusoidally perturbated around its steady-state value at a given frequency:

$$p(t) = \bar{p}\,\{1 + A\,\sin[\omega(t - t_0)]\}, \qquad t \geq t_0$$

with

$$\omega = 2\pi f$$

$$f = 0.8a_0/2L = 0.4a_0/L$$

$$A = 0.05$$

The other boundary conditions are unchanged from the steady-state computations. In particular, the constant mass flow rate and total enthalpy conditions correspond to a nonzero wall admittance. Simple algebra yields $(v'/p')_{inj} \simeq -\bar{v}/\bar{p}$ or, expressed in dimensionless form,

$$Y = \frac{\rho_0 a_0}{\gamma}\frac{v'}{p'} = -\bar{M}_{inj}\frac{p_0}{\bar{p}} = -0.00267$$

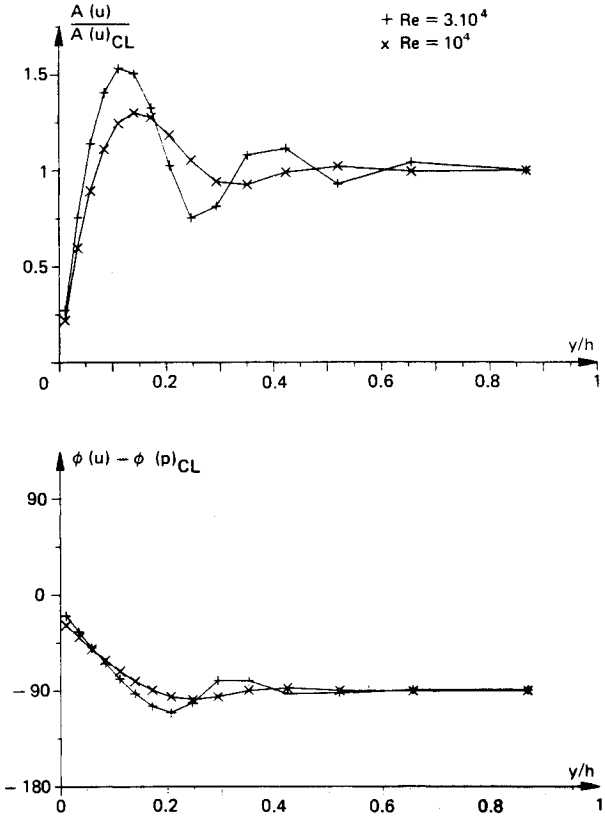

Fig. 4 Transverse profiles of parallel acoustic velocities from Ref. 5.

With reference to the experimental work of Ref. 10, the forcing frequency has been chosen close to the first acoustic mode frequency. This choice is sufficient to have an acoustic pressure node inside the chamber.

Figure 2 shows the chamber pressure time history, from chamber pressurization to the beginning of the forced regime. Figure 3 shows the velocity predicted at chamber midlength. It is possible to see that a stationary unsteady regime (standing wave) is typically established after 7–8 oscillation periods, and that the oscillation amplitude is low enough to avoid marked acoustic nonlinear effects, which were not the purpose of the present work. Once the standing wave pattern is established, three more periods of excitation are performed with an imposed constant time step (here $\Delta T = 0.00070$, close to $0.6\Delta T_{CFL}$), and the Fourier coefficients of all flow variables U at the forcing frequency are computed according to

$$FT(U) = \frac{1}{3T}\int_0^{3T} U(t)\,\exp(i2\pi ft)\,\mathrm{d}t$$

with T being the time period of the excitation, $T = 1/f$. Then, the amplitudes and phases of acoustic components are derived from the modulus and phase of $FT(U)$:

$$A(U) = \mathrm{Mod}\,[FT(U)]$$

$$\phi(U) = Arg[FT(U)]$$

All the computed results, therefore, have the form of these acoustic components that are directly comparable to available analytical linear results.[5,7] Unsteady computations with the fine grid were run on ONERA's CRAY XMP 18 supercomputer and required roughly 270 s of CPU for computing one cycle of oscillation (3571 time steps). A fully vectorized version of the computer code has since cut the computing time by a factor of approximately eight.

Preliminary unsteady computations were also performed with the coarse grid on a Cyber 855 and required 250 s of CPU

for one cycle of oscillation (1785 time steps). It was then possible to assess the influence of the grid size on the results.

Discussion of Results

Most of the present results concern the acoustic velocity fields and the corresponding acoustic boundary layers. The most striking feature of such acoustic boundary layers lies in the tangential velocity transverse profile. This profile shows a strong velocity overshoot close to the injection surface, together with a large phase advance, relative to the core of the flow. Examples of such profiles obtained from a simple analytical model[5,6] using the conditions given above are shown in Fig. 4 for two reference Reynolds numbers. For the case of $(Re)_0 = 3.10^4$ corresponding to the present numerical computations, the acoustic velocity overshoot is slightly more than 50% of the external velocity and the phase advance is of the order of 60 deg. It can be seen in Fig. 4 that this simplified model predicts that, for $(Re)_0 = 3.10^4$, the boundary layer would extend into the entire chamber volume.

These acoustic velocity profiles are features of an unsteady shear wave, which is created by unsteady viscous forces and which propagates away from the injecting wall. Shear wave characteristics can be easily analyzed for the case of a purely transverse mean flow (no axial velocity) and for a linear unsteady field.[5,6] Further refinements of the mean flowfield description lead to great analytical complexities.[7] Nevertheless, the simplified analysis, which should be exact in the vicinity of the injecting wall ($u \simeq 0$), shows that the shear wave length and shear wave spatial attenuation are strong functions of two parameters: 1) F, the ratio of injection to acoustic Reynolds numbers, which fixes the number of shear wave length present in the boundary layer

$$F = \frac{v_{inj}/\nu}{\sqrt{\omega/2\nu}}$$

and 2) a characteristic viscous wave number

$$\beta = \sqrt{\omega/2\nu}$$

that defines the physical size of the boundary layer. For $F \gg 1$, the viscous zone is dominated by the injection (transverse convection), and the number of shear wave length is found to vary roughly like $F^2/2$, while boundary thickness varies like F^3/β and shear wave length like F/β.

For situations typical of solid rockets, F is of the order of 5–10. Such large values of F lead to a slightly damped shear wave. Moreover, for the given injection Mach number and viscosity, a larger motor means a lower characteristic frequency and thus both a lower β and a larger F. This leads to a thick boundary layer consisting of a slightly damped shear wave. For many applications, this analysis leads to unrealistic acoustic boundary-layer thicknesses (of the order of, or larger than, the chamber transverse dimensions) invalidating the whole simplified theoretical approach. The main difference between this simplified theoretical analysis and real-life situation lies in the mean flow description. Since the transverse mean flow velocity component, which convects the shear wave, must vanish at the center line of the motor, acoustic boundary-layer extension must be somewhat limited. It is believed that the present full numerical computations should lead to a more realistic description of acoustic boundary layers representative of rocket motor situations.

The present computations correspond to $F = 2.91$ and $\beta L \simeq 371$, which lead to relatively thick boundary layers due to an artificially low reference Reynolds number (μ was chosen to be roughly 100 times its laminar value for a 1-m motor and with reference speed of sound of 1000 m/s), chosen for demonstration purposes. However, this set of parameters was chosen to lead to an acoustic boundary layer that extends into the core of the flow, a situation that is believed to be representative of large rocket motors.

Present Numerical Results

All the predicted behavior is in the form of moduli and phases of acoustic components at the forcing frequency. The phase origin was arbitrarily set at 90 deg for the pressure at the head-end of the chamber. The first results to be mentioned concern the transverse acoustic pressure profiles. The pressure wave was found to be purely planar, with no detectable transverse acoustic pressure gradients (neither in modulus nor in phase angle). This result is contradictory to recent numerical results published by Baum[9] for a traveling pressure wave. This comparison indicates that, for the case studied here, the refraction/diffraction phenomenon of a traveling pressure wave by the mean flow gradient, exactly cancels between upstream and downstream propagating waves. As it turns out, this phenomenon may not be an important feature of classical acoustic instability regimes. However, this point should be more thoroughly analyzed for the case of rocket motors sustaining strong, nonlinear instability at higher frequencies.

Figures 5 and 6 present axial, center plane, profiles of acoustic pressure, and axial velocity as computed on both grids. It should be noted that in Fig. 5 the pressure amplitudes are expressed relative to the reference pressure p_0. This pressure is 3.67 times lower than the mean operating pressure $\bar{p}$ due to chamber pressurization. Clear evidence of a standing wave pattern is visible, with a pressure node located roughly at $x/L = 0.60$. The benefit of enhanced spatial resolution brought by the fine grid is also visible, although the coarse grid results seem acceptable at this point. These profiles, which are evaluated away from the injecting wall and from the unsteady viscous zone, closely resemble classical one-dimensional results.

Figure 7 presents the transverse profiles of the axial component of the acoustic velocity that can be compared to the simple analytical profiles presented in Fig. 4 for $(Re)_0 = 3.10^4$. The moduli are normalized to the center plane value, while the phases are expressed relative to the acoustic pressure phase at center plane. This figure shows that the the coarse grid is not able to correctly capture the secondary overshoot due to poor spatial resolution. It is also interesting to note that both grids

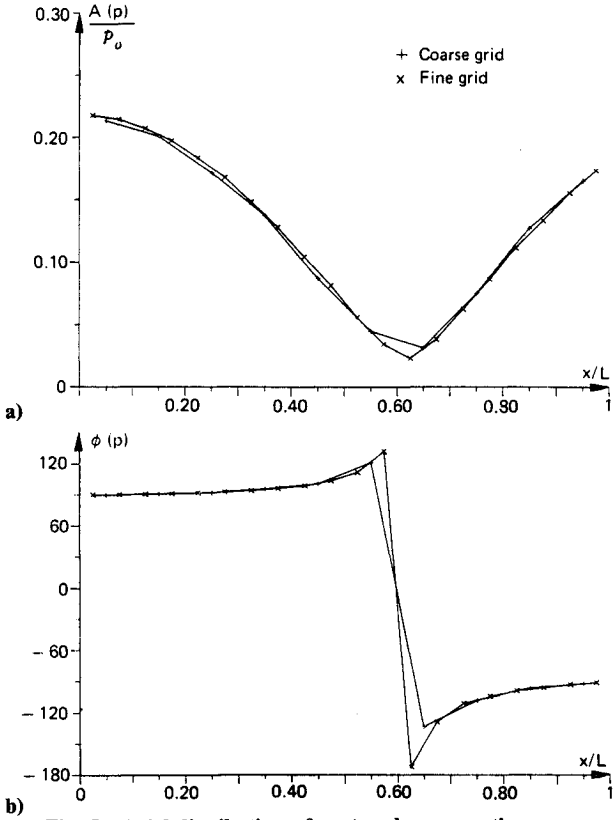

Fig. 5 Axial distribution of center plane acoustic pressure.

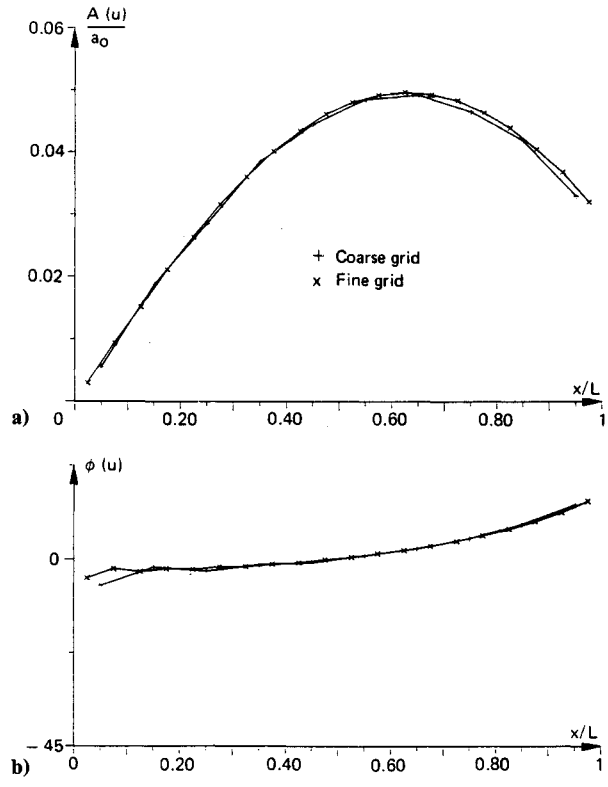

Fig. 6 Axial distribution of center plane axial acoustic velocity.

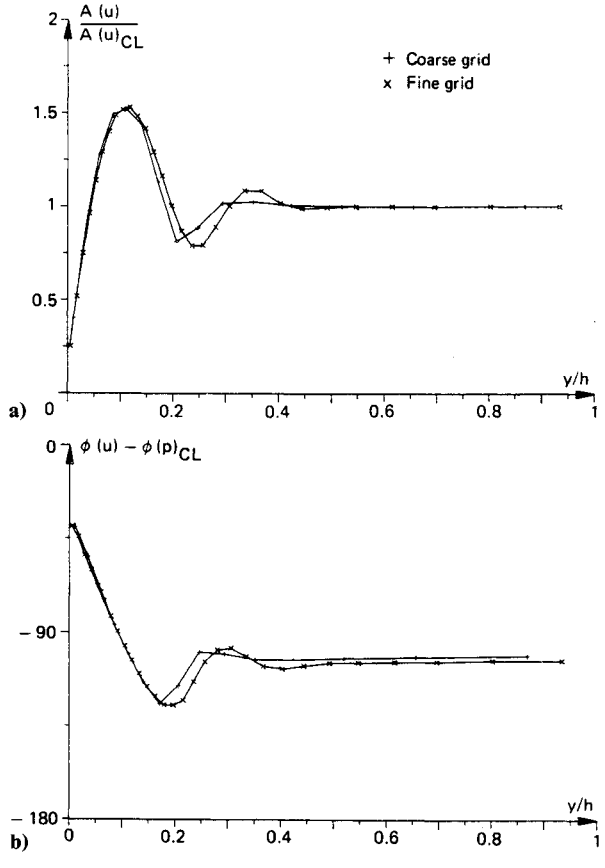

Fig. 7 Transverse profiles of parallel acoustic velocities at chamber midlength.

permit the capture of the first part of the shear wave, indicating that the fine grid is presumably overconcentrated near the injection surface for the chosen set of parameters (mainly frequency, viscosity, and injection velocity). It must also be noted that the computed profiles on the fine grid recover those

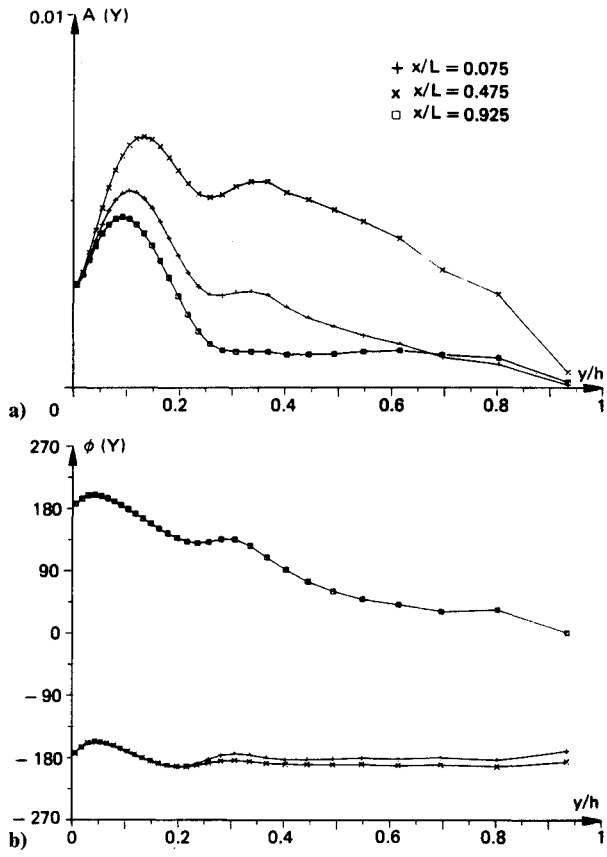

Fig. 8 Transverse profiles of Y ($Yw = -0.00267$).

of the simple analytical model in the vicinity of the wall, i.e., the same value and location of the first overshoot and the same value of the phase shift at the wall.

Figure 8 presents the fine grid variations of local dimensionless acoustic field admittance, defined as $Y = \rho_0 a_0 v'/\gamma p'$, across the chamber at different axial locations. It is interesting to note that the values of the field admittance vanish at the center plane, due to the symmetry condition ($v = 0$) imposed there. Moreover, it must be noted that the field admittance is found to vary with the axial coordinate, as one moves away from the injecting wall. Identical values are found at the wall, due to the chosen boundary conditions. Indeed, the constant mass flow rate and total enthalpy conditions lead to a constant wall admittance $Y_w = -0.0027$ that is recovered by the plots of Fig. 8. Hence, the observed axial variation of the acoustic field admittance is an effect of the boundary layer proper and of its interactions with the mean flow, since it cannot be linked to change in the wall admittance. The phase angle profiles plotted in Fig. 8 show different behavior between head-end and aft-end regions. Indeed a 180-deg phase difference is found to exist between wall and center plane in the aft-end, while an almost constant phase angle is found in the head-end region. The phase profiles indicate that there exist, in the aft-end part of chamber, regions where the real part of the acoustic field admittance is positive implying positive $p \cdot v$ work. However, it should be emphasized that the downstream boundary condition (mainly a planar pressure wave) may be affecting the reported results due to an uncontrolled acoustic energy interaction. This point will be cleared as soon as full motor (including the nozzle) unsteady computations become available. Figure 9 illustrates axial variations of the acoustic field admittance as observed on the fine grid and at a fixed height above the wall ($y/h = 0.306$), located at the edge of the zone of rapid transverse variations. Marked variations are observed with a maximum located at the pressure node (see also Fig. 5).

Different behavior is found upstream and downstream of this location; higher field admittance is found in the head-end

region. Positive real parts of the field admittance are found in the chamber domain $0.65 \leq x/L \leq 0.85$. The dashed line in Fig. 9 represents the admittance at the edge of the boundary layer as computed by means of the simplified analysis,[5,6] which corresponds to the so-called flow turning losses. Three remarks can be made at this point: 1) flow turning losses are usually considered as a surface term; it is clear from Fig. 8 that this is not the case due to boundary-layer extension; 2) the value of this admittance is predicted to be constant along the chamber length, which is far from the full solution results; and 3) the admittance value obtained by means of the simplified analysis is significantly different from the values derived from the present results.

The present results concerning admittance variations along the chamber with a maximum at the pressure node location recover the analytical results of Hegde et al.[7] It should be

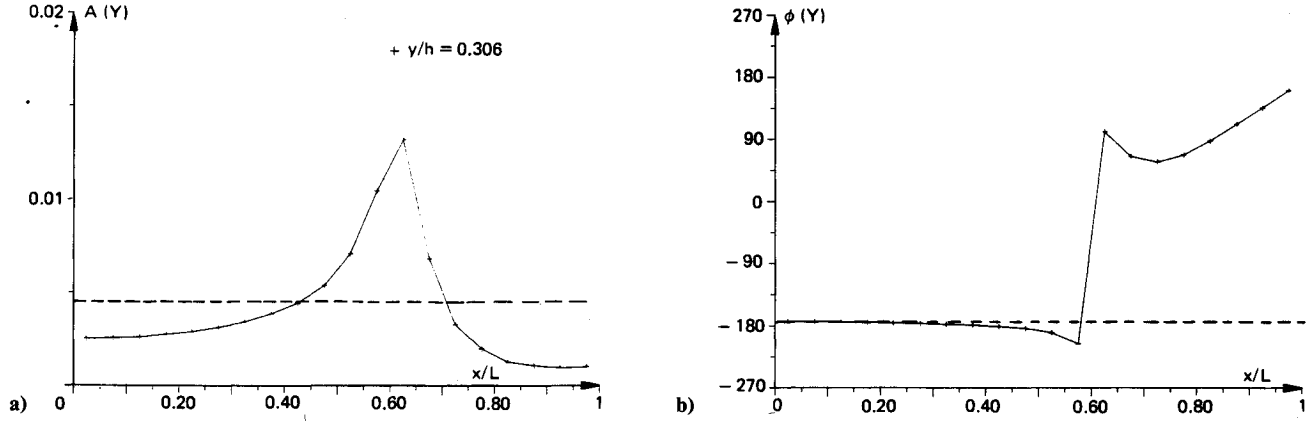

Fig. 9 Axial distribution of Y for $Yw = -0.0027$ (the dashed line predicted by simplified analysis).

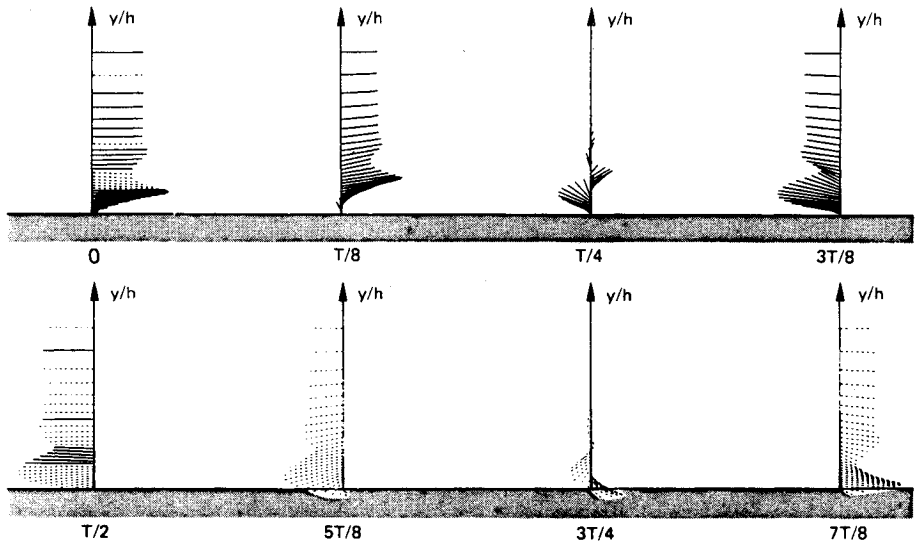

Fig. 10 Instantaneous acoustic velocity profiles at head-end ($I = 2$) (vertical velocities magnified by 3).

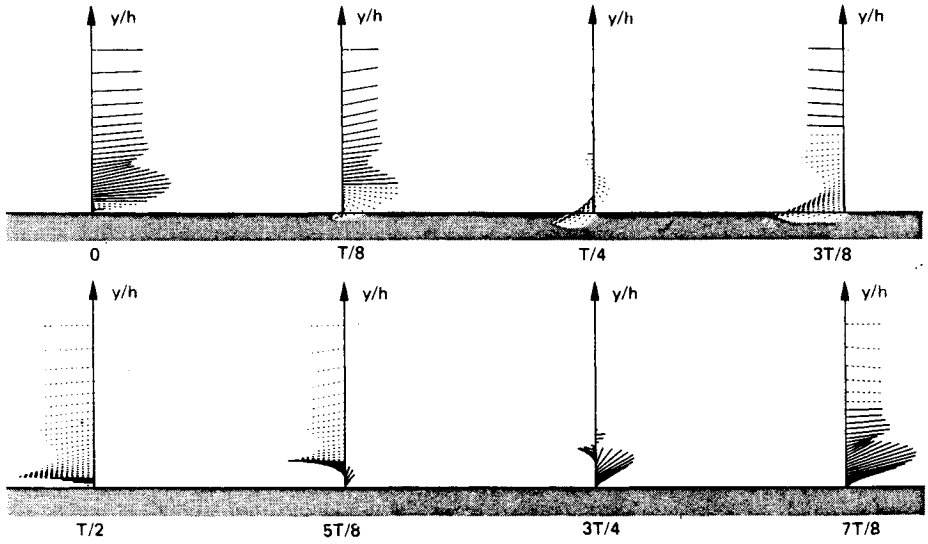

Fig. 11 Instantaneous acoustic velocity profiles at aft-end ($I = 18$) (vertical velocities magnified by 30).

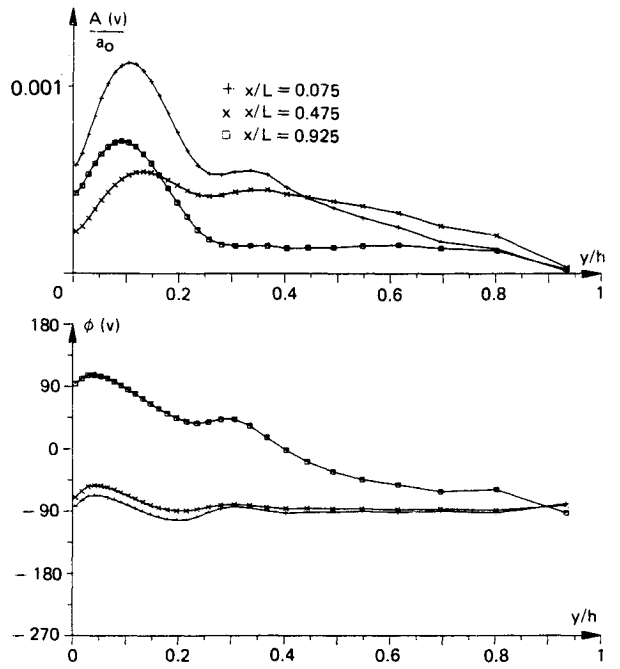

Fig. 12 Transverse profiles of normal acoustic velocities ($Yw = -0.0027$).

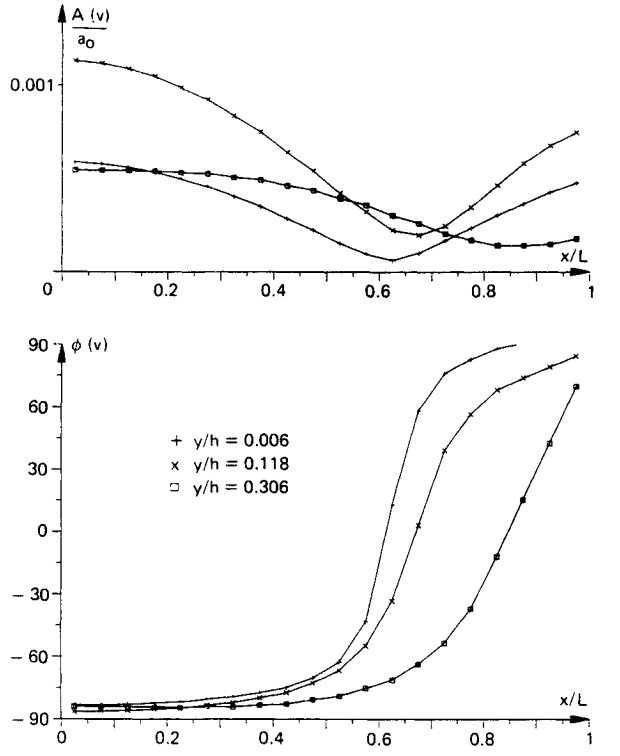

Fig. 13 Axial distribution of normal acoustic velocity.

stressed that this result is essential to proper evaluation of solid rocket motor stability.

Other results concern the vortical nature of the acoustic field. The vorticity is introduced by the shear wave and has been ignored by most present time stability analysis. First consideration of this rotational nature of the acoustic velocity field is given in Ref. 16. According to the present work, the classical hypothesis of an irrotational acoustic field (e.g., in the form of $\boldsymbol{u}' \sim \boldsymbol{grad}\ p'$) built in many existing stability prediction codes is highly questionable for situations where large unsteady viscous zones are anticipated (this is particularly crucial for large motors whose characteristic frequencies

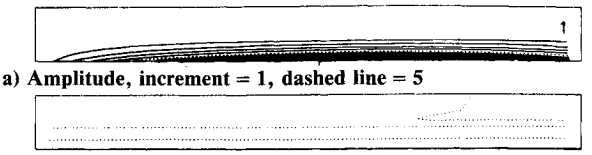

a) Amplitude, increment = 1, dashed line = 5

b) Nodal lines $\Phi = 0$

Fig. 14 Dimensionless acoustic vorticity maps.

are extremely low). Figures 10 and 11 show computed acoustic velocity vectors across the chamber height at two axial locations and at several times into the oscillation cycle. Dashed vectors correspond to negative (toward the injecting wall) transverse velocities. It is visible in Fig. 10 that, in the head-end region, one main vortical cell exists, whereas, in the aft-end region (see Fig. 11), two contra-rotating cells are found. This latter result corresponds to experimental (cold flow) data obtained by Brown et al.[16]

This important finding can be further analyzed with the help of transverse and axial profiles of the transverse acoustic velocity displayed in Figs. 12 and 13. Figure 12 shows that at $x/L = 0.925$, a 180-deg phase shift exists in the transverse velocities between wall and center plane, while further upstream, v' is almost in phase across the chamber height. Figure 13 shows that the axial minimum of the transverse velocity is displaced downstream as one moves away from the injecting surface, resulting in the observed 180-deg phase shift. This behavior is believed to be an effect of the mean flowfield becoming more axially dominant.

Figures 14a and 14b present maps of the acoustic vorticity modulus and phase computed from the following complex expressions:

$$\Omega' = -\left[\frac{\partial A(u)}{\partial y} + iA(u)\frac{\partial \Phi(u)}{\partial y}\right]e^{i\Phi(u)} + \left[\frac{\partial A(v)}{\partial x} + iA(v)\frac{\partial \Phi(v)}{\partial y}\right]e^{i\Phi(v)}$$

Analysis of the numerical solution indicates that the main contribution to Ω' is brought by the first term relative to $\partial/\partial y$. The dimensionless vorticity modulus, $|\Omega'| = |\Omega'^*|L/a_0$ (where * denotes dimensioned vorticity), reaches a value of 12 at the wall (see Fig. 14a) and near the acoustic pressure node. Its phase angle is found to vary linearly across the chamber height, except for $x/L > 0.80$ where a secondary contrarotating cell of weak strength appears, below the center plane. Figure 14b shows the nodal lines of $\Phi(\Omega')[\Phi(\Omega') = 0]$. It is interesting to note that these acoustic vorticity maps differ slightly from the incompressible, inviscid results establishing that Ω and Ω' must be conserved on any streamline. A nonnegligible diffusion of unsteady vorticity is observed towards the injecting surface.

Conclusion

The present work is an attempt to describe fully the acoustic boundary layer that develops above the burning propellant of a solid rocket motor. The full numerical solution of two-dimensional, laminar, compressible, unsteady Navier-Stokes equations permits the full features of solid rocket motor two-dimensional mean flowfield to be incorporated in the analysis. The presented results concern a standing acoustic wave regime that is established through pressure forcing at a given frequency. A special Fourier treatment permits the numerical results to be put in a form that allows comparisons with classical available linear acoustic data used by design engineers for predicting solid rocket motor stability margins.

Presented results indicate that the simplified analytical treatment of acoustic boundary layers correctly predicts the tendencies. However, such an analysis is found inappropriate for many cases of interest where thick boundary layers are

predicted. Indeed, the full Navier-Stokes solution shows that the mean flow gradients lead to a thinner boundary layer and to boundary-layer acoustic field admittances that vary along the chamber length. Moreover, the acoustic field is found to be rotational over a significant volume of the chamber interior, a result that invalidates the presently available stability prediction codes based on the irrotational acoustic balance approach.

It must also be stressed that, according to the present calculations, many solid rocket motor designs are predicted to have large unsteady viscous zones, which may lead to a volume flow turning loss, rather than the classical surface term. The influence of this result on rocket motor stability prediction is not yet well understood. More work is still needed before arriving at reliable solid rocket motor stability predictions.

Finally, full understanding of a burning propellant response to velocity fluctuations requires further analysis of acoustic boundary layer and ad hoc modeling of turbulence characteristics in an acoustic field. The presented results, although limited to laminar regimes, indicate that the acoustic velocity field in a solid rocket motor is much more complex than envisioned by any velocity coupling model, especially with respect to the large velocity overshoot and phase advance that have been found to exist in the vicinity of the burning propellant.

Acknowledgments

This work has been supported by contracts from Direction des Recherches et Etudes Techniques du Ministère de la Défense, DRET-Gr. VII.

References

[1]Hart, R. W., and McClure, F. T.; "Theory of Acoustic Instability in Solid Propellant Rocket Combustion," *10th International Symposium on Combustion*, Combustion Inst., Pittsburgh, PA, 1965, pp. 1047–1065.

[2]Culick, F. E. C., "The Stability of One-Dimensional Motions in a Rocket Motor," *Combustion Science and Technology*, Vol. 7, 1973, pp. 165–175.

[3]Culick, F. E. C., "Stability of Three-Dimensional Motions in a Combustion Chamber," *Combustion Science and Technology*, Vol. 10, 1975, pp. 109–124.

[4]Van Moorhem, W., "Flow Turning in Solid Propellant Rocket Combustion Stability Analyses," *AIAA Journal*, Vol. 20, No. 10, 1982, pp. 1420–1425.

[5]Flandro, G. A., "Solid Propellant Acoustic Admittance Correction," *Journal of Sound and Vibration*, Vol. 36, No. 3, 1974, pp. 297–312.

[6]Vuillot, F., and Kuentzmann, P., "Flow Turning and Admittance Correction: An Experimental Comparison," *Journal of Propulsion and Power*, Vol. 2, No. 4, 1986, pp. 345–353.

[7]Hegde, U. G., Chen, F., and Zinn, B. T., "Investigation of the Acoustic Boundary Layer in Porous-Walled Ducts with Flow," *AIAA Journal*, Vol. 24, No. 9, 1986, pp. 1474–1482.

[8]Baum, J. D., and Levine, J. N., "Numerical Investigation of Acoustic Refraction," *AIAA Journal*, Vol. 25, No. 12, 1987, pp. 1577–1586.

[9]Baum, J. D., "Acoustic Energy Exchange Through Flow Turning," AIAA Paper 87-0217, Jan. 1987.

[10]Avalon, G., Pascal, J., and Cauty, F. "Experimental Investigation of a Type of Solid Propellant Velocity Coupling," AIAA Paper 87-1727, July 1987.

[11]Lengellé, G., "Model Describing the Erosive Combustion and Velocity Response of Composite Propellants," *AIAA Journal*, Vol. 13, No. 3, 1975, pp. 315–322.

[12]T'ien, J. S., "Oscillatory Burning of Solid Propellants Including Gase Phase Time Lag," *Combüstion Science and Technology*, Vol. 5, 1972, pp. 47–54.

[13]Flandro, G. A., "Non-Linear Transient Combustion of a Solid Rocket Propellant," AIAA Paper 83-1269, June 1983.

[14]Beddini, R. A., and Robert, T. A., "Turbularization of an Acoustic Boundary Layer on a Transpiring Surface," AIAA Paper 86-1448, June 1986.

[15]Brown, R. S., Blackner, A. M., Willoughby, P. G., and Dunlap, R., "Coupling Between Acoustic Velocity Oscillations and Solid Propellant Combustion," *Journal of Propulsion and Power*, Vol. 2, No. 5, 1986, pp. 428–437.

[16]Brown, R. S., Blackner, A. M., Willoughby, P. G., and Dunlap, R., "Coupling Between Velocity Oscillations and Solid Propellant Combustion," AIAA Paper 86-0531, Jan. 1986.

[17]Traineau, J. C., Hervat, P., and Kuentzmann, P., "Cold Flow Simulation of a Two-Dimensional Nozzleless Solid Rocket Motor," AIAA Paper 86-1447, June 1986.

[18]Avalon, G., and Vuillot, F., "Prévision du Comportement Instationnaire d'une Tuyère Amorcée," Office National d'Etudes et de Recherche Aérospatiales, TP 1988-149, AAAF 25e Colloque d'Aérodynamique Appliquée, Bordeaux, France, Oct. 1988.

[19]Baum, J. D., and Levine, J. N., "A Critical Study of Numerical Methods for the Solution of Non-Linear Hyperbolic Equations for Resonant Systems," *Journal of Computational Physics*, Vol. 58, No. 1, 1985, pp. 1–28.

[20]Santosa, F., and Pao, Y. H., "Accuracy of a Lax Wendroff Scheme for the Wave Equation," *Journal of Acoustics Society of America*, Vol. 80, No. 5, 1986, pp. 1429–1437.

[21]Culick, F. E. C., "Rotational Axisymmetric Mean Flow and Damping of Acoustic Waves in a Solid Propellant Rocket," *AIAA Journal*, Vol. 4, No. 8, 1966, pp. 1462–1464.

[22]Dunlap, R., Willoughby, P. G., and Hermsen, R. W., "Flowfield in the Combustion Chamber of a Solid Propellant Rocket Motor," *AIAA Journal*, Vol. 12, No. 10, 1974, pp. 1440–1442.